Effects of Nanoindentation Loading Rates on Pop-in Events and Deformation Mechanisms in Single-Crystal Zinc

V.N. DOAN, S. KUCHARSKI, and M. MAJ

Single crystals of pure zinc were examined using instrumented spherical indentation on the basal-oriented surface at three different loading rates. The residual impressions and the surrounding surface were investigated using atomic force microscopy and electron backscatter diffraction in order to reveal information about the topography and orientation changes. Noticeable pop-ins were reproducible in the majority of the tests. Contrary to reports in the literature, the pop-in initiation load and loading rates were found to have an inverse relationship, and this behaviour was attributed to twinning deformation and dislocation movement. In tests with all loading rates, evidence of twinning could be found both within and outside of the imprints. Residual impressions composed of slip and twin 'subgrains' and external twins manifested as sink-in patterns were observed in most of the tests, and the difference lay in the dissimilar twin formations at different loading rates. A hypothesis was developed to address the change in deformation behaviour within the subsequent loading process after a pop-in event.

https://doi.org/10.1007/s11661-026-08311-y

I. INTRODUCTION

DURING load-controlled nanoindentation, a phenomenon called 'pop-in', characterised by a sudden burst of indentation displacement, is often reported. The first occurrence of pop-in is widely considered to mark the start of plastic deformation; prior to this, deformation is entirely elastic and can be fitted with a Hertzian prediction curve. For this reason, the stress at which the first pop-in occurs is considered to represent the critical resolved shear stress for any mode of plastic deformation.[1,2]

The change in the behaviour of a material due to a variation in the loading rate is a manifestation of a phenomenon known as strain rate sensitivity (SRS). Two aspects of SRS can be observed in indentation tests. The first is the effect of the loading rate on pop-in event at the onset of plasticity, and the second is the influence on strain hardening (hardness) and secondary pop-in in the fully plastic regime.

The handling Editor for this article was Jian-Feng Nie and the handling Associate Editor was Yoon Suk Choi.

V.N. DOAN, S. KUCHARSKI, and M. MAJ are with the Institute of Fundamental Technological Research, Warsaw, Poland. Contact e-mail: skuchar@ippt.pan.pl

Manuscript submitted April 2, 2026; accepted July 6, 2026.

The incipient plasticity in nanoindentation tests depends on temperature and loading rate, and to explain this relationship, dislocation nucleation mechanisms were analysed in great detail.[3,4] One report for this behaviour was made by Schuh *et al*.[4] based on nanoindentation results for single-crystal platinum. Homogeneous dislocation nucleation was ruled out as a likely mechanism; instead, heterogeneous nucleation sites were suggested to be controlling incipient plasticity. A hypothesis was proposed that the first displacement burst is governed by a low-energy process (the activation energy provided in the research was 0.28 eV) at the scale of a point defect and occurs at a fraction of atomic sites (the activation volume provided was less than a cubed Burger's vector]. On the basis of nanoindentation test and micro-pillar compression tests on two different Mo-alloy single crystals, it was confirmed that compared to homogeneous sources of dislocation, heterogeneous mechanisms have lower energy barrier to overcome.[5] The dependence of onset of plasticity in HEA over similar loading rate and temperature ranges (25 to 2500 μN/s, 25 to 150 °C) was examined in nanoindentation tests by Zhu *et al*.[6] The decrease of pop-in load with increasing temperature was observed, while the increase of loading rate leads to the increase of pop-in load. The extracted activation energy and volume from experimental results were also used to determine that heterogeneous dislocation nucleation mediated by vacancies or vacancy-like defects was favoured over homogeneous nucleation. The higher activation energy and volume values than conventional FCC metals were

Published online: 30 July 2026

attributed to the fact that the vacancy migration in this work concerns several atoms. Mason *et al*.[7] recorded pop-in loads (incipient plasticity) for loading rates over the range of 25 to 2500 μN/s at three different temperatures in a Berkovich indentation tests on single-crystal platinum. The tendency for pop-in to occur at higher loads under elevated loading rates was found across the range of temperatures considered in these tests. The viability of homogeneous and heterogeneous dislocation nucleation mechanisms was analysed.

In Reference 8, the complex influence of the tip radius, loading rate, presence of pre-existing dislocations and crystal orientation was investigated experimentally in Ni_3Al alloy, using blunt Berkovich tips with radii of 50 and 160 nm. At a radius of 160 nm, the pop-in load and length were about 0.24 mN and 6 nm, the maximum resolved shear stress reached 0.092G, where G is shear modulus, and approached the theoretical shear stress of $G/2\pi = 0.159G$. For the smaller tip, the first pop-in appeared at a resolved shear stress that was only slightly greater than that for the larger tip. In these tests, the pop-in load corresponded to the incipient plasticity and was a result of homogeneous nucleation of dislocation loops. The effect of the loading rate was not examined. In addition, for the smaller tip, "major pop-ins", during plastic deformation regime, were observed on the loading curve at a much higher load (7 mN), and also on the unloading curve at approximately 2 mN. This was explained by the existence of locked dislocations in Kear–Wilsdorf configuration that formed prior to the major pop-in event could act as a pinning point, stopping other dislocations from gliding. However, the super kink (edge dislocation) can break free of the lock and act as a Frank–Read source for dislocation generation. The resulting movement will produce a pop-in event. Thus, the major pop-ins in this work were considered to be of heterogeneous origin. It was observed that during loading, the pop-in load became larger and the pop-in length diminished as the loading rate increased. This was associated with the time required for the growth of dislocation loops.

The phenomenon that the pop-ins having different origin was also investigated in Reference 9 on the basis of medium entropy alloy. Their hypothesis stems from the result that the distribution of critical shear stress corresponds to the first pop-in event has a statistical nature, which was illustrated to be multimodal. This finding suggested that multiple sources are responsible for dislocation nucleation phenomenon. By thoroughly analysing the volume of stress and the distance between the various crystalline defects present in the studied material, different mechanisms of dislocation nucleation were determined and assigned to each distribution peak accordingly. The influence of other factors such as local chemical order (LCO) on micro-yielding mechanisms was investigated in Reference 10 with nanoindentation pop-in tests. Furthermore, by utilising statistical analysis of pop-in events, three different dislocation-based mechanisms corresponding to these events, which incipient plasticity coincides with, were identified.

A number of previous works concerning SRS are listed in Table I, the majority of which were made on the basis of indentation on FCC or BCC metals, single- and poly-crystals, where sharp tips (usually Berkovich or conical tips) were applied at very low loads. Therefore, the tests were considered to be spherical indentation with a small tip radius (50 to 300 nm). Plastic deformation was usually accommodated by slip. A positive SRS was observed, with pop-ins occurring at higher loads when the loading rate increased.

A somewhat less frequently reported scenario is the inverse effect of the loading rate on the pop-in load, which can be found in research involving GaAs and Si in Reference 14. The pop-in load and subsequently the contact pressure in the experiment on GaAs were found to have a negative relationship with loading rate. This result stands in contrast to reports for many other materials as mentioned above, and it was stated by the authors that the incipient plasticity corresponding to the pop-ins could be attributed exclusively to the phase transformation process rather than to dislocation nucleation, as the former requires less energy.

The plastic deformation modes of HCP metals are more complex, as both slip and twinning systems may be activated. Investigations of pop-in events presented in many papers focus on discussing these two deformation mechanisms for different indentation directions.[19] The indentation tests were performed on a scale that is different to that used in the above-discussed SRS investigations (Table I). That is to say, spherical indentation was performed using tips with radii in the range of several micrometres (3 to 10 μm). Residual impressions were examined using EBSD and/or AFM to detect twins. Within this category of experiments, magnesium and its alloys were examined far more frequently than zinc. SRS was not investigated in the context of these deformation modes. However, the effect of temperature was investigated,[20] where it was found that the load corresponding to the first pop-in (incipient plasticity) decreased with increasing temperature in magnesium alloys. It was concluded that the pop-in event only occurs when twinning takes place, which is triggered by dislocation nucleation.

One of the few existing studies on the effect of loading rate on Zn tests was conducted on polycrystalline zinc samples using standard sheet tensile specimens.[21] It was demonstrated that true stress increases with true strain rate, while strain rate sensitivity decreases with strain rate. The mechanical properties of zinc are examined using indentation test in several papers. SRS of polycrystalline zinc was investigated in Reference 22. In nanoindentation tests (sharp tip), a greater hardness was observed at smaller penetration depths, and this was attributed to a greater indentation strain rate at these depths. Pop-in events were not observed. In bulk compression tests, an increase in strain rate was associated with an increase in yield strength. This behaviour was attributed to zinc's deformation mechanism being dominated by diffusion-mediated deformation due to its high homologous temperature. One study of zinc mechanical properties was carried out by Nguyen *et al*.,[23] who used a sphero-conical tip with a radius of 1 μm on a zinc polycrystalline sample. They then compared the results with a crystal plasticity model.

Table I. Summary of SRS Investigations in Nanoindentation Tests Presented in Literature

Examined material	Tip Used	Tip Radii	Loading (Strain) Rates	SRS
$Ti_{60}(AlCrVNb)_{40}$[11]	Berkovich tip	215 nm	10 to 500 μN/s	positive
Mg and Mg Alloys[12]	cube corner tip	X	10, 1, 0.1 and 0.02 mN/s	positive
Nanotwinned Cu[13]	pyramidal sharp tip	X	0.01, 0.025, 0.05 and 0.125 s^{-1}	positive
GaAs[14]	spherical tip	840 nm	3, 1 and 0.5 mN/s	negative
Mg–Gd–Y–Zr[15]	Berkovich tip	X	5×10^{-3} s^{-1} to 1 s^{-1}	negative
Ni and Mo[16]	blunt Berkovich tip	220 nm	from 10 to 2430 μN/s	neutral
Tantalum[17]	Berkovich tip	X	1000 and 5000 μN/s	neutral
Ta Single Crystal[18]	Berkovich tip	190 nm	50 and 5000 μN/s	neutral

This approach was applied to study the effect of cold rolling on nanoindentation response of zinc.[24]

The mechanical response of zinc was explored more thoroughly by Sarvesha *et al.* in Reference 25 using spherical indentations with a spherical radius tip of radius 10 μm. For indentation on the (0001) plane, complete pile-up with a quasi-regular hexagonal shape was observed, while for the other orientations (pyramidal, prismatic), pile-up and sink-in in the form of a characteristic cross-sectional valley were generated. Moreover, grain fragmentations, or formations of subgrains, were found inside residual impressions away from the basal orientation. Indentation in the basal plane was associated with the stiffest *P-h* curves and the smallest pile-up resulting from the second-order pyramidal slip system activated which exhibit high strain hardening. Basal slip was also activated, although unlike indentation on the non-basal planes, the presence of twins was not observed. Deformation modes for indentation on the pyramidal and prismatic planes were found to be similar to each other, in which three deformation systems were activated including slip on the basal and second-order pyramidal planes and contraction twinning.

Other properties of zinc, such as creep, were reported in References 26, 27, while the elastic modulus was experimentally determined in References 26 through 28 for basal, prismatic and pyramidal oriented grains. Single-crystal zinc with low level of existing dislocations (after etching and annealing) was investigated in Reference 29 using nanoindentation tests with spherical tips of different radii. It was observed that pop-in events generated two distinct groups of crystallographic cells within the imprint: (i) 'slip subgrains', exhibiting a maximum misorientation of approximately 14 deg, and (ii) 'twin subgrains', characterised by a misorientation of approximately 86 deg. This misorientation corresponds to $\{10\bar{1}2\}$ $\langle 10\bar{1}\bar{1} \rangle$ twins, which, in zinc (c/a = 1.856), are compression twins. These structural changes are associated with a specific pile-up/sink-in pattern that can be correlated with pop-in displacement.

The deformation mechanisms of zinc in nanoindentation tests have generally not been studied as intensively as those of other hexagonal close-packed (HCP) materials, such as magnesium and its alloys. In particular, the effect of loading rate on pop-in events has not been systematically explored. This study demonstrates how the mechanical response of zinc, as presented in Reference 29, is affected by the loading rate. We conducted nanoindentation tests on a single zinc crystal, applying three different loading rates at room temperature. We systematically analyse and categorise the strain rate sensitivity of zinc with regard to major pop-in events and microstructural changes to the material beneath the indenter based on the results of the experiments. We show that zinc exhibits negative strain rate sensitivity (SRS), which is associated with twinning and slip plasticity during pop-in events. The plastic deformation of zinc after pop-in was briefly discussed.

II. EXPERIMENTAL DETAILS

High-purity (99.9999 pct) single-crystal zinc, produced via the Czochralski method, was acquired from MaTecK GmbH (Germany) in the form of a rod 14 mm in diameter. The rod was cut into smaller samples of ~ 5 mm in height, perpendicularly to the rod axis (where the rod axis was parallel to the c-axis of the crystal) using a wire saw, in order to obtain a relatively even surface with minimal damage. Samples were annealed at 200 °C for two hours at a heating rate of 5 °C/min and then cooled down in the furnace to further reduce the dislocation density from the previous process. The effect of the annealing on the presence of pop-in events was explored by Miller *et al.*[30] for thin gold films; in their study, pop-ins were observed for annealed samples, while they were absent from the as-deposited specimen.

A pop-in displacement burst occurs when nanoindentation is performed on a material with a low local dislocation density in the surface region.[31–36] The likelihood of pop-in events decreases as the density increases. One common explanation for this is that plastic deformation can initiate at existing defects, reducing the requirement for new dislocations to nucleate. This results in a low elastic limit and a smooth transition from elastic to plastic deformation without any significant interruption to the indentation P-h curve. Additionally, an increase of density of pre-existing dislocations may lead to greater plastic stiffness in the material, as manifested by a lower slope in the P-h curve. One possible cause of pre-existing dislocations is surface preparation, as described in references.[37–39] As Pathak *et al.*[40] phrased it, pop-in can be 'avoided' by mechanically altering the surface even in small degree, which can cause some 'undesirable effects' such as surface hardening.[41,42] For this reason, mechanical polishing should not be applied when examining the pop-in phenomenon. It should also be noted that after such polishing, the density of defects and the state of the material are not precisely known. Therefore, another reason for avoiding mechanical polishing is to eliminate this uncertainty and obtain *P-h* curves, showing a repeatable distribution of pop-in loads.

In the present study, electro-polishing with chromic acid as the electrolyte was used to reduce surface roughness and remove hardened and/or oxidised layers. This was followed by preliminary nanoindentation tests. This sequence was repeated to check whether subsequent etching altered the shape of the *P-h* curves. The procedure was finished when the P-h curves following two consecutive etchings almost coincided. Prepared surfaces were examined with a light microscope and an atomic force microscope for flat areas of reasonably large size and a mean roughness (Sa) of 1 to 3 nm. The samples were preserved in a desiccator between experiments. The annealing and electro-etching processes ensure that we examine a material in a precisely defined state that can easily be replicated in other laboratories.

Load–penetration curves were measured using nanoindentation tests performed with a UNHT tester (Anton Paar Open Platform Equipment) and a spherical indenter with a radius of 9.2 μm. The results for the tip calibration are presented in Reference 43. The maximum measured load range was $F = 0$ to 50 mN and the depth was $h = 50\ \mu$m. The load and displacement resolution were 2.5 nN and 0.0005 nm, respectively. All of the tests were performed using a load-controlled process.

AFM (Nanit AFM, Nanosurf AG, Switzerland) was used to scan the residual imprints after the nanoindentation tests, and Gwyddion software was used to analyse the 3D topography maps and to specify the gradients of the measured surfaces. Presenting surfaces in terms of their gradients reveals features such as small areas with different slopes and heights, which manifest as small steps at common boundaries. In particular, the contact boundary between the indenter and the specimen and/or the sink-in boundary is visible. To show such features, we apply this mode of presentation to the selected imprints.

Indentation tests were carried out on the basal plane (0001) of zinc single-crystal sample, using three different loading rates of 0.5mN/min, 5mN/min and 80mN/min. The holding time between loading and unloading was 2 seconds. Contact was detected using an indenter force sensor at loads ranging from 0.005 to 0.001mN. The spacing between individual indents corresponded to between six and eight residual impression diameters. The maximum applied load is not fixed and is set at 10 to 25mN. For selected tests, the maximum load was assumed to be lower than 25mN (i.e. 10 to 16mN) in order to terminate the loading process almost immediately after the pop-in event. This makes it possible to compare the two states of residual impressions: the first corresponding to the deformation directly after pop-in, and the second when loading continues after pop-in and the deformation increases.

The experiments were repeated for different samples at each loading rate, to verify the repeatability of the results, in view of the scattering in the pop-in displacement and pop-in load values. After the indentation tests, the crystallographic orientation of the residual impressions was examined using the EBSD method with a Zeiss CrossBeam 350 scanning electron microscope equipped with a Hikari Super EBSD camera. The acceleration voltage and beam current were 22 kV and 2.2 nA, respectively. A step size of 40 nm was used to produce all EBSD maps.

III. RESULTS

A. *Analysis of Exemplary Imprints for Different Loading Rates: P-h Curves and Summary of Pop-in Events*

The pop-in events are statistically characterised by their occurrence at specific frequencies within certain load ranges, which are specific to the given loading rate. Examples of *P-h* curves exhibiting pop-in events are shown in Figure 1 for loading rates of 0.5, 5 and 80 mN/min. TheP-h curves for the lowest loading rate are presented as dotted lines and marked as 'LR'; in the case for the medium loading rate, the curves are in the form of dashed lines and are named as 'MR', whereas for the highest loading rate indents, they are shown as continuous lines and are marked as 'HR'. The parts of the curves before pop-in do not show significant differences between different rates; the deviation arises from the pop-in events, to be specific, a substantial pop-in event for each indentation curve. An observation can be made that pop-ins occurred at lower loads and with lower displacement for high loading rate indents, with exceptions such as imprint HR_3 in fewer numbers. For low loading rate indentation, the pop-in load can sometimes be found to be higher than 15mN, which was not recorded for other loading rates; therefore, to present these imprints in Figure 1, a higher maximum load is needed. After pop-in, the sample continues to deform

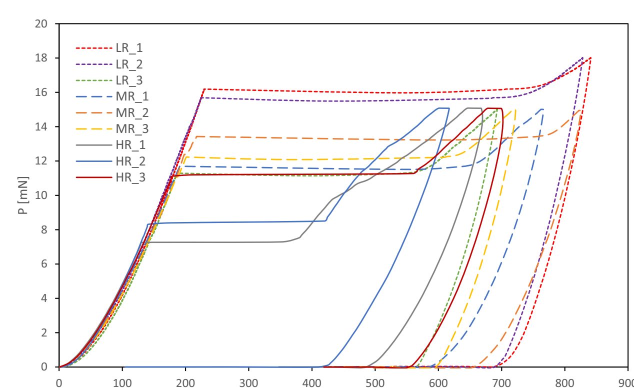

Fig. 1—Exemplary *P-h* curves for loading rates: 0.5 mN/min (LR), 5 mN/min (MR) and 80 mN/min (HR).

plastically with subsequent loading, as shown by the near-linear response in the load–displacement curves.

Creep deformation was observed for indentations at all loading rates during the holding period and was more pronounced for indents performed at higher loading rates. A simple explanation may be that the loading time after pop-in to the maximum load for lower rate indentation is longer than at the higher rate. Creep can be easily exhausted over a longer loading time, and only a small degree can be observed during the holding period.[44]

The pop-in initiation loads were plotted against displacements for all recorded occurrences, as presented in Figure 2. To create this plot, at least 80 results for each loading rate were collected. This summary suggests that pop-ins occur at a lower load for higher loading rate indentations, and this effect is consistently observed in our research. It is worth remarking that our results indicate that the pop-in initiation load and loading rate have a negative correlation; this is seldom reported in the literature and will be addressed in the discussion section of this paper. Furthermore, the trend that pop-in occurs at higher load and is necessarily accompanied by higher displacement is evident both in our data and in previous research.[3,45–47]

The distributions of pop-in displacement versus pop-in initiation load are shown in Figures 3(a), (b) and (c) for loading rates of 0.5, 5 and 80 mN/min, respectively. While pop-in events are inherently stochastic during indentation, certain load ranges exhibit a higher probability of occurrence. Under similar experimental conditions, the load range that has the highest amount of recorded pop-in events for loading rate of 20mN/min was reported in Reference 29 to be 8 to 9 mN; however, the larger dataset in that study allowed the concentration of pop-in events to be identified more clearly. Two notable details in Figure 3 should be addressed. The first one is regarding the histogram of pop-in load for the low loading rate indents, which appears to have more than a single load ranges with higher number of results. This is different from the other loading rate results. An explanation for this can be due to the lack of adequate number of indents needed in order to identify the most populated pop-in initiation load range, for this loading rate, group has the lowest

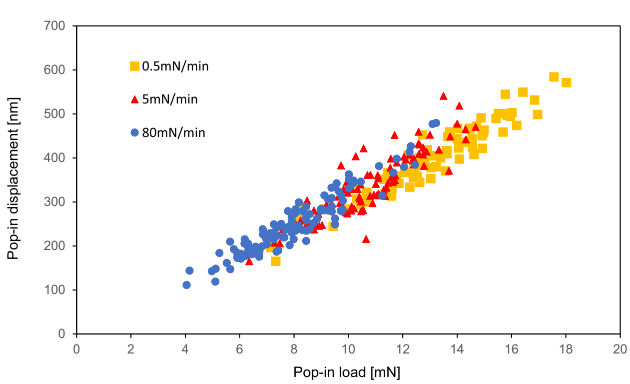

Fig. 2—Pop-in load plotted against pop-in displacement of experiments for all loading rates.

number of recorded results in our work. The second detail is the rather stronger dispersion pop-in displacement contributed by a small number of imprints for medium loading rate group. These results should be considered outliers, and the origin for these indents can be derived from their locations, due to uncertainty that is the defect densities underneath the indenter, which cannot be fully controlled during surface preparation. These outlier imprints probably were made at locations with particularly unique volume of defects that can influence the pop-in displacement. Nonetheless, the primary goal of the presented results is to indicate that the pop-in initiation load shifts towards higher load as loading rate increases, or in other words, it is sensitive to the loading rate.

In all graphs, the left sides (at lower loads) have fewer results compared to the right sides (at higher loads). This may suggest that under a certain load value, it is less likely or even unlikely for pop-ins to manifest in our experiments.

B. *Topography and EBSD Analysis of Exemplary Indents*

3D AFM measurements of exemplary indents made at different loading rates are shown in Figures 4, 5 and 6, for rates of 0.5, 5 and 80 mN/min, respectively. For experiments of low loading rate, a test named LR_4, whose P-h curve (although not displayed in Figure 1) almost coincides with that of indent LR_3 and has similar pop-in load and displacement values as well, is presented in Figure 4 alongside LR_3. The residual impressions of these two imprints show remarkable resemblance to each other qualitatively. Within the maximum load range, for all loading rates, the majority of the results show a combination of hillocks and cross-sectional valleys, forming specific pile-up/sink-in patterns. The sink-ins are also known as 'bird wings', due to their distinctive shape. A scheme to describe the sink-in pattern is displayed in Figure 4(b), where length is estimated as the sink-in profile reaches the normal surface, and depth is estimated from the point at which the sink-in profile begins to show roughness until it reaches the normal surface. This assumes that the sink-in portion did not come into contact with the indenter, meaning that the roughness was not flattened. The term 'valley' will be used as a synonym to sink-in pattern occasionally in our work to avoid over repeating one term. This response has previously been reported for zinc[25] and magnesium;[48] however, this peculiar shape was not observed in indentation tests on the basal plane in Reference 25 and was correlated with the absence of significant pop-ins during these tests. For zinc, sink-in was associated with twinning deformation, while pile-up was produced by dislocation slip.[25] In the present study, the 'bird wings' can be observed to be longer when a lower loading rate is applied. Moreover, as shown in the profiles for low and medium loading rate imprints in Figures 4(b), (d) and 5(b), (d), respectively, the pile-up and sink-in formations appear to be more distinct when compared to those of high loading rate indents, Figures 6(b), (d); in other words, a diminished

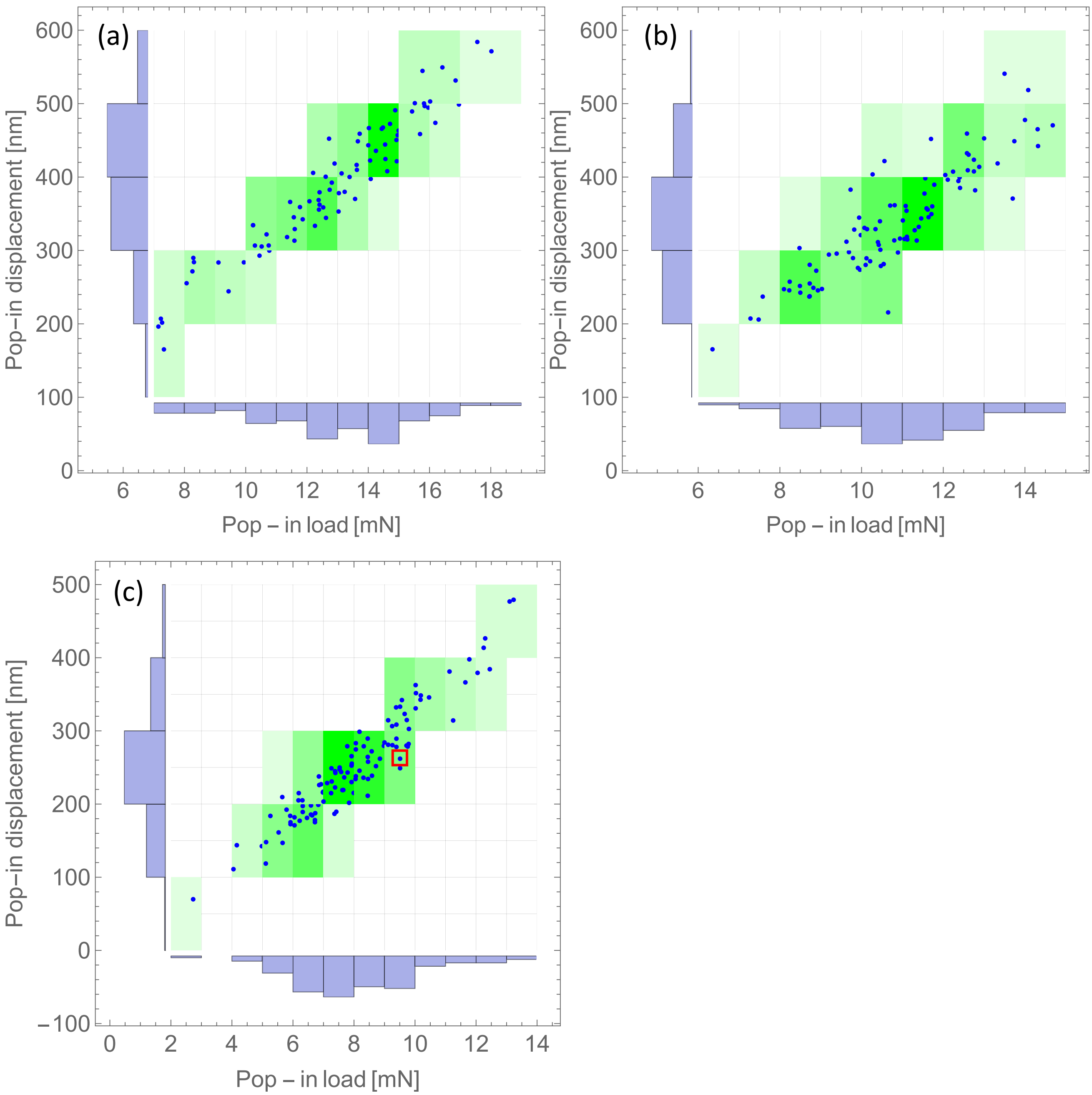

Fig. 3—Distribution graphs of pop-in initiation load the respective displacement that show the load ranges that pop-ins are more likely to occur for (*a*) 0.5 mN/min, (*b*) 5 mN/min, and (*c*) 80 mN/min tests. The marked imprint with a red rectangle is imprint HR_6.

volume of deformation was recorded outside of the residual impression for the higher loading rate imprints. In the case of indent HR_3 in Figures 6(c), (d), the bottom was cut at 200 nm from the deepest point in the presentation to highlight the sink-in area, which is otherwise minuscule and difficult to distinct it, the same treatment was applied to the profiles of this residual impression.

Further analysis was done on the selected imprints with the EBSD technique, and the results are shown in Figures 7(a), (b), (c), (d), and (e), (f) for indents at low, medium and high loading rates, respectively. Evidence of twinning is found both within the residual impression and in the sink-in areas. The identified twinned cells have misorientation of about 86 deg, which corresponds to compression twinning for zinc,[49] causing contraction along the c-axis. The standout result is the EBSD measurement of indent HR_3, which will be discussed below. Moreover, the basal plane crystal structure was provided for each EBSD measurement at the top right corner of all IPF maps. The valley (sink-in) is generated in the direction [$\bar{1}2\bar{1}$ 0] and this direction coincides with that of the twin structure (bird wing) formed outside the residual impression, Figures 7(a) through (d). In

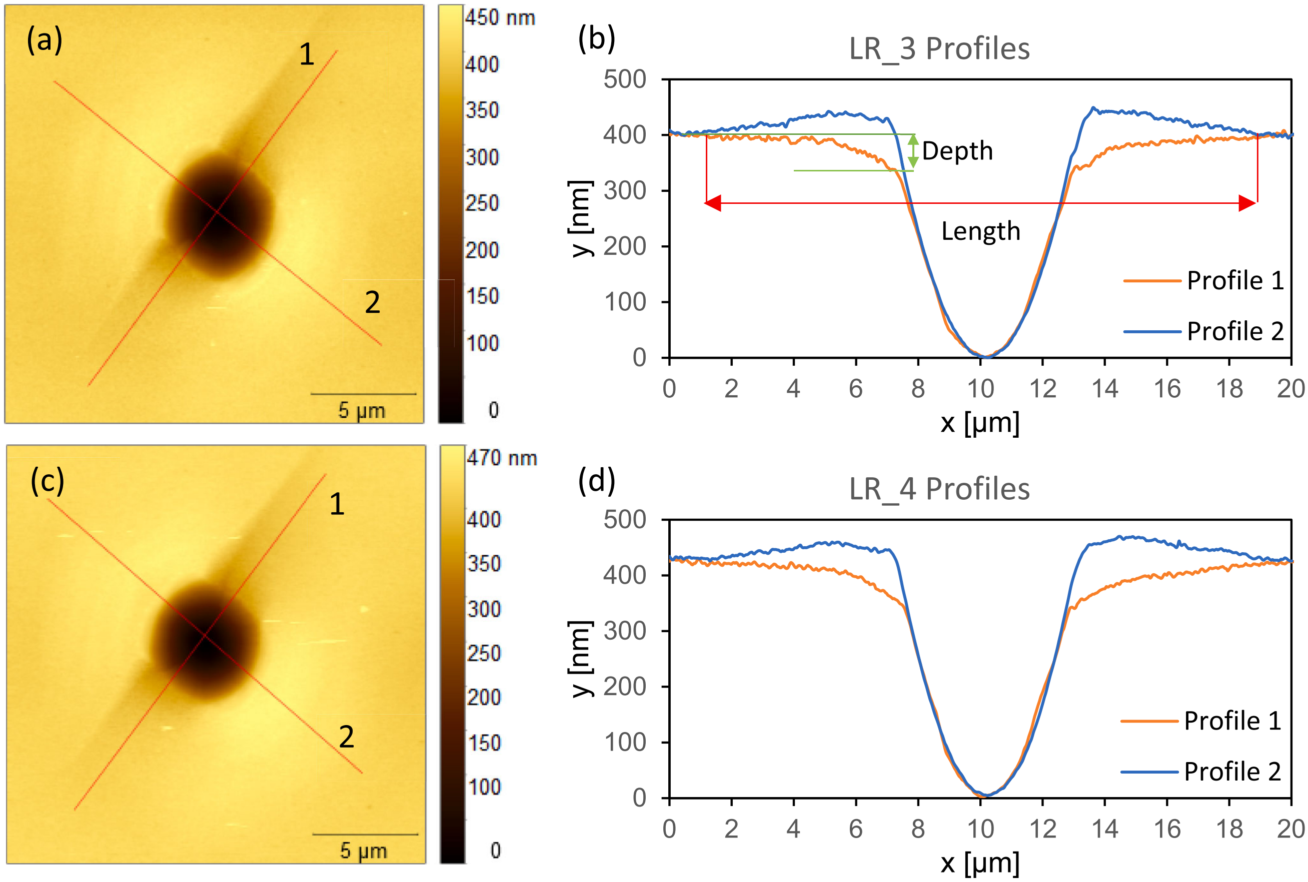

Fig. 4—AFM measurements of 0.5 mN/min loading rate indents (*a*) LR_3, (*b*) its profiles, and (*c*) LR_4, (*d*) its profiles.

Figure 7(e), no twin outside of the contact area was found, but the twin structure can be found to be elongated parallel to the direction $[\bar{1}2\bar{1}0]$.

It is important to note that there is permanent material displacement outside of the twinned regions, which gives credence to the hypothesis that other mechanisms also take place in addition to the deformation provided by the twin. Thus, significant slip must accompany twinning during the pop-in burst. The notion that pop-in events are due to a combination of slip and twinning has also been reported in other works, with similar results found in References 20,29,48. In Reference 29, unloading was performed immediately after pop-in, or pop-in occurred during the holding time, thus minimising the additional deformation beyond the excursion in some indents. EBSD measurements indicated a complex texture on the surface, with both twin and slip cells, not dissimilar to that shown in Figure 7.

This combination of deformation mechanisms can be found in both the sink-in regions and within the residual impressions that came into contact with the indenter. Within the sink-in areas, twinned material does not correspond to the entire wing in both length and width, but is instead associated with the deeper portions of the birdwing. Moreover, in view of Figures 7(a) through (d), the detected twin evidently forms a single cell apart from the remaining portion of the valley, which retains a similar orientation to the undeformed surface in our observation, suggesting that this area is deformed purely by slip. This stands in contrast to the deformation behaviour in the contact area of the residual impression, where both slip and twin structures are in the form of multiple cells.

For the lowest loading rate indents, the EBSD measurements show substantial twin deformation in the form of the bird wing. This portion is the greater than those of higher loading rates imprints. A shared detail between the two examples in Figures 7(a), (b) is the large and seemingly single cell in the centre of the residual impressions, which has basal plane orientation. This result indicates that the dislocation slip was the deformation mechanism at this location. The twin structure displayed on the surface formed into two sections. The first one is inside the residual impression along the sink-in direction; this twin formation should extend from one side of the bird wing to the other. The other twin section is located on the opposite site of the residual impression across the deformed by dislocation slip cell in the centre.

For the examples of indent at the loading rate of 5mN/min, shown in Figures 7(c) and (d), deformation by twinning is favoured in the direction of the valley; similarly to the low loading rate imprints, twin structure is divided into cells with a slight misorientation relative to each other. Twin structures can be found outside of the sink-in direction and are somewhat connected to the

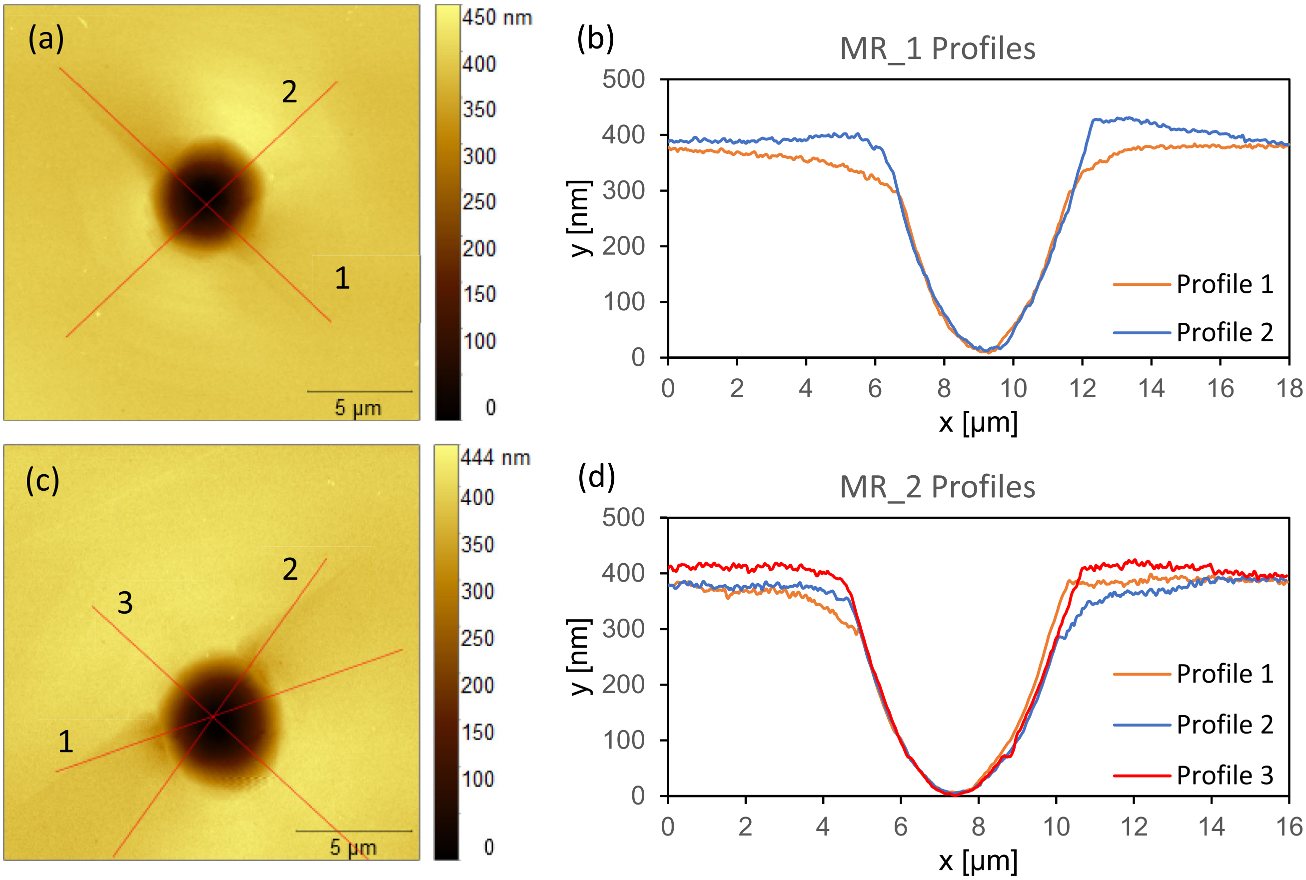

Fig. 5—AFM measurements of 0.5 mN/min loading rate indents (*a*) MR_1, (*b*) its profiles, and (*c*) MR_2, (*d*) its profiles.

major twinned area. The deformation mechanism is not limited to twinning; as remarked above, as sections deformed by dislocation slip also form into cells. For imprint MR_1, Figure 7(c), the imprint structure is not divided into regions of complete twinning or complete slip, since a small slip cell is seen in Figure 7(c) in between the twin formation. Nevertheless, cells that share a similar deformation mechanism seem to aggregate and form two large areas of distinctly different crystallographic orientation. For imprint MR_2, Figure 7(d), which has rather large pop-in load and displacement for indentation of medium loading rate, the structure of this imprint is more similar to that of low rate imprints as shown in Figures 7(a) and (b) than imprint MR_1, where a single cell at the centre is surrounded partially by twinned material. Although there are some differences, such that the twin structure on the left side is not as extensive, as well as lesser bird wing size. This is in spite of the fact that its pop-in load and displacement are both greater than those of the lower rate indents.

It has come to our attention that the results for 5 mN/min loading rate imprints are quite comparable to previous works in Reference 29, in which the nanoindentation tests were performed at the loading rate of 20 mN/min, while the results for the high loading rate imprints are different from those in some key points, an example of which is shown in Figure 7(e), imprint HR_1. The first difference is that no twin was detected in the sink-in region compared to the results for the lower loading rates. This corresponds to a valley region that is neither as deep nor long as for the lower loading rates, Figure 6(b), as remarked previously. Twin structure can be detected inside the residual impression in the direction of sink-in, not dissimilar to that of other loading rates results. A more special case of the 80mN/min loading rate is indent HR_3, which has high pop-in load initiation load and displacement values. As mentioned above, the AFM measurement in Figures 6(c) and (d) showed a small and diminished sink-in pattern. This small sink-in can be correlated with the sliver area of twin in the bottom left section. The sink-in and this sliver of twin is also in the direction $[\bar{1}2\bar{1}0]$, which is similar to all other examples. The twin area in the sink-in does not connect to twin structure within the contact boundary. The twins inside the residual impression take the form of many branches that protrude into the portion of the imprint deformed by slip, which in turn produces a rather complicated twin boundary shape compared to other examples.

C. *Imprints with Very Low Increase of Load After Pop-in Event*

In this section, we present and discuss the imprints that were unloaded almost immediately after pop-in for

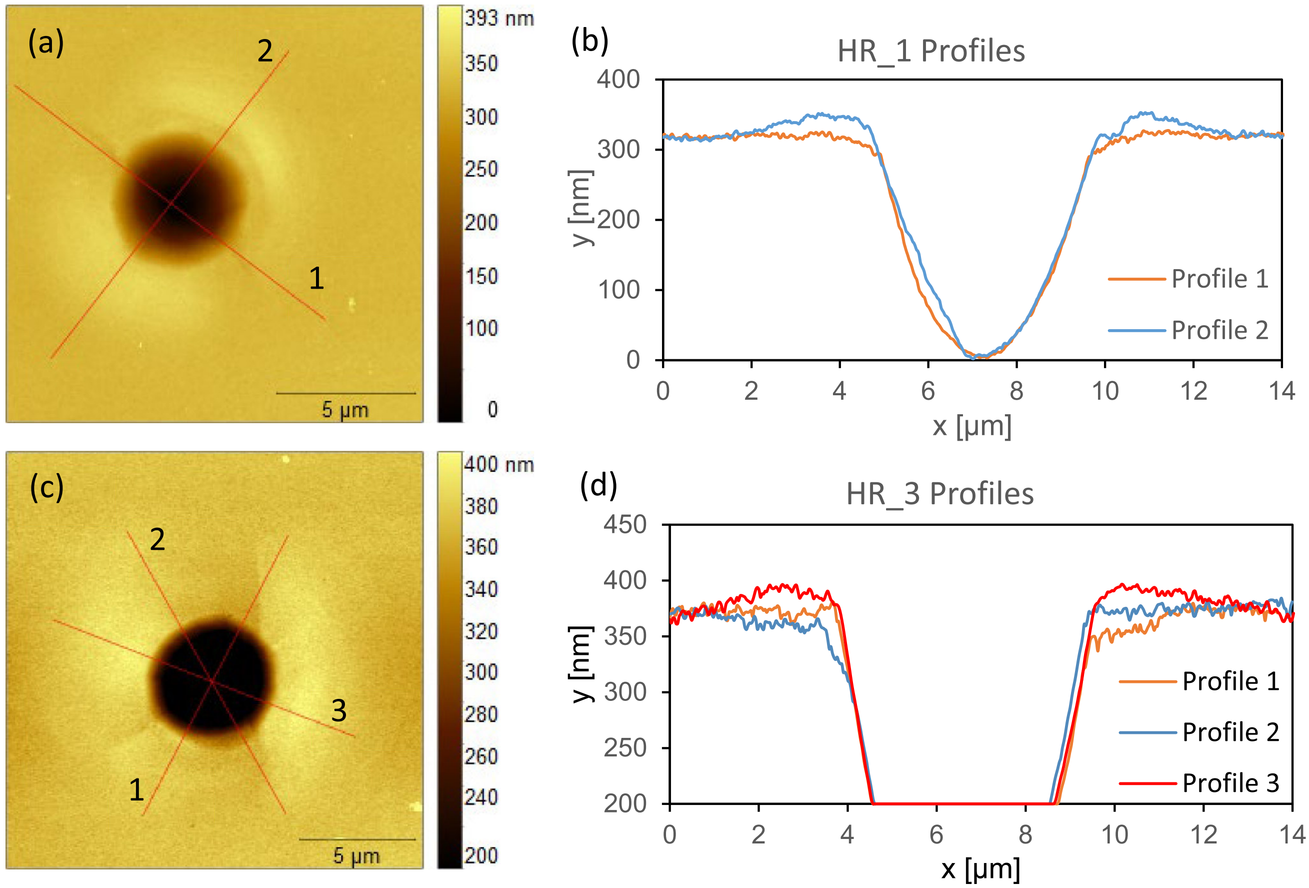

Fig. 6—AFM measurements of 80 mN/min loading rate indents (*a*) HR_1, (*b*) its profiles, and (*c*) HR_3, (*d*) its profiles.

all loading rates, whose *P-h* curves are shown in Figure 8.

For 5 mN/min 80 mn/min loading rate imprints, there is a small increase of load after the end of pop-in events. This was due to 'indenter speed up' phase where the indenter accelerated to maintain the designated loading rate, as well as a small loading portion that occurred subsequently. In order to minimise the displacement caused by the recovery phase, a higher recording frequency of 100 Hz (instead of 10 Hz for the rest of the data) was applied to both of the higher loading rate experiments, so that the unloading process can be registered with greater accuracy. Thus, the pop-in events here have a slightly different shape compared to those in Figure 1. However, pop-in load and displacement registration at different recording rates in our experiment was found to have quite insignificant differences. The displacement induced by these final portions of loading is estimated to be less than 30 nm for these two groups. For low loading rate imprints, the process of 'indenter speeding up' is much milder due to the ease to maintain the loading rate by the equipment. Therefore, high recording rate is not needed in this case. Furthermore, for 0.5mN/min loading rate indentation, such high recording rate would produce an overwhelming amount of without providing much more useful information. For this reason, the lowest loading rate experiments here were recorded in 10 Hz frequency.

AFM measurements in the form of gradient maps (derivative of the Z value with respect to the X axis, referred to as the "gradient map") of residual impressions of the imprints in Figures 8(a), (b), and (c) are shown in Figures 9, 10 and 11, respectively. It can be seen that, for imprints that have large pop-in events, the sink-in and pile-up topography features can be observed even when very little load was applied after the displacement burst. The observation of sink-in in this work is consistent with the results reported in Reference 29, where the sink-in was found to form during the pop-in event. Both the sink-in and pile-up become less distinct for results of higher loading rates. At the highest loading rate, these patterns are the least distinct in depth (or height) from the normal surface. For the low loading rate imprints, the AFM measurements show results that have decent similarities between them, despite the difference in their pop-in loads and displacements. Within the contact boundary, there is a certain shape in the direction of the valley in imprint LR_5 and LR_6, this shape is not as evident for imprint LR_7. In the case of other loading rates, only imprint MR_6 and HR_6 have notable topography features along the direction of sink-in.

Despite having pop-in at different initiation loads, the EBSD measurements of low loading rate imprints [Figure 8(a)] show considerable agreements with each other. The similarities extend to the results previously

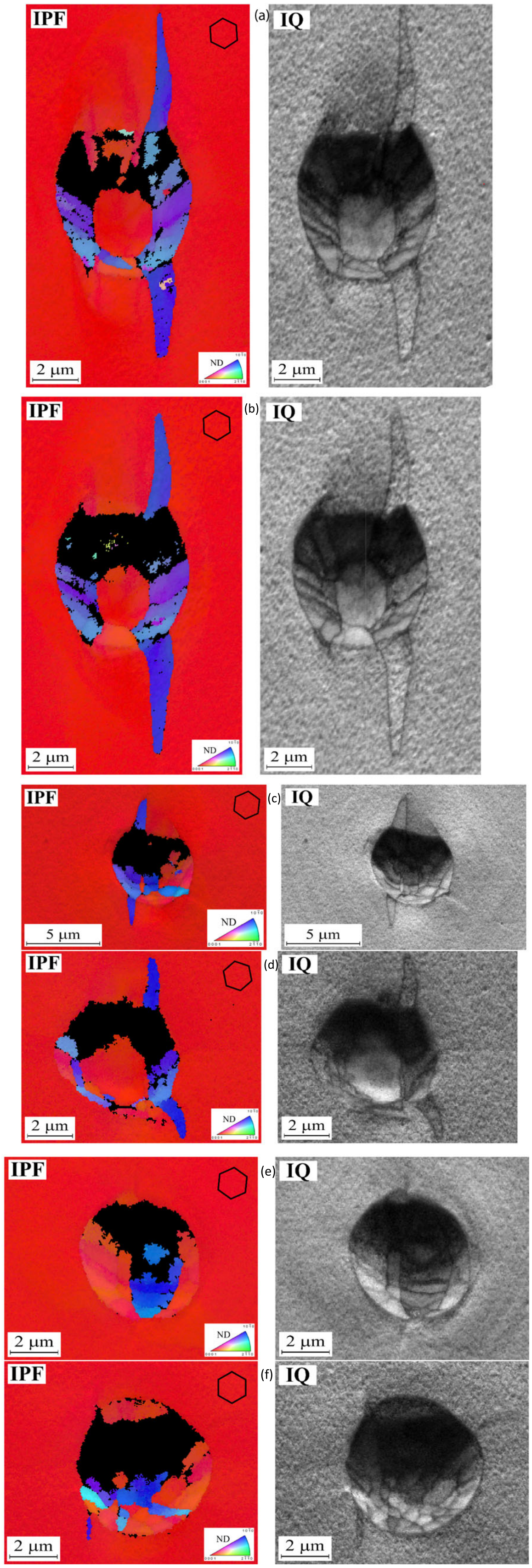

◀Fig. 7—Maps for the residual impressions obtained from EBSD measurements: misorientation map (IPF) and image quality map (IQ), (*a*) LR_3, (*b*) LR_4, (*c*) MR_1, (*d*) MR_2, (*e*) HR_1, and (*f*) HR_3.

presented for imprints LR_3 and LR_4, which have slightly lower pop-in load and were under load for longer time after pop-in event. EBSD results of imprints MR_4 and MR_5, Figure 8(b), show a familiar twin structure in the direction of sink-in previously presented in Figures 7(c) and (d). Twin structure of imprint MR_6 [Figure 8(b)] is somewhat different as it does not extent continuously from one side of the bird wing to the other. However, twinned area is still more concentrated close to the sink-in pattern. Imprints HR_4 and HR_5 have comparable pop-in events to each other [Figure 8(c)], the load at which pop-in occurred (about 10 mN) is higher than that of imprint HR_1 (7.26 mN) but lower than the value of imprint HR_3 (11.13 mN). On one hand, the twin structures of the two tests are similar to each other, and twinned area in the sink-in direction is not continuous like what is seen in Figure 7(e). On the other hand, twin cells can be found scattering in the residual impression in between untwined ones.

Imprint HR_6 is a rather special case, as have been described above, and it has twin area on the surface solely concentrated within the residual impression. This twin structure almost connects the two small bird wings, yet no twinned material was found within the sink-in. The topography feature shown in the AFM measurement [Figure 11(c)] can be correlated to this twin structure. The minute sink-in pattern can be treated similarly to the tip of the large sink-in, which does not show evidence of twinning deformation in our research. The explanation for this can either be detwinning occurred post-indentation or such amount of deformation does not require twining as the deformation mechanism. The EBSD measurement of this imprint is quite similar to that of imprint HR_1 [Figure 7(f)] in terms of twin pattern. Although the origins of the twin patterns might differ. Imprint HR_1 had significant loading after pop-in. According to the results in Reference 29, the sink-in portion develops during the pop-in event and does not expand further during subsequent loading. When the contact area increases, the sink-in becomes 'engulfed' and disappears. This should have been the deformation sequence for imprint HR_1. In indent HR_6, very low amount of load was applied after the pop-in, this indicates that the sink-in corresponding to its displacement burst is quite miniscule., and was not reduced by the subsequent increase of load.

IV. DISCUSSION

A. *Deformation at Pop-in Event*

Based on the results presented in Result section of this work, the observation of twin structure on the surface can be correlated to the displacement burst. In other

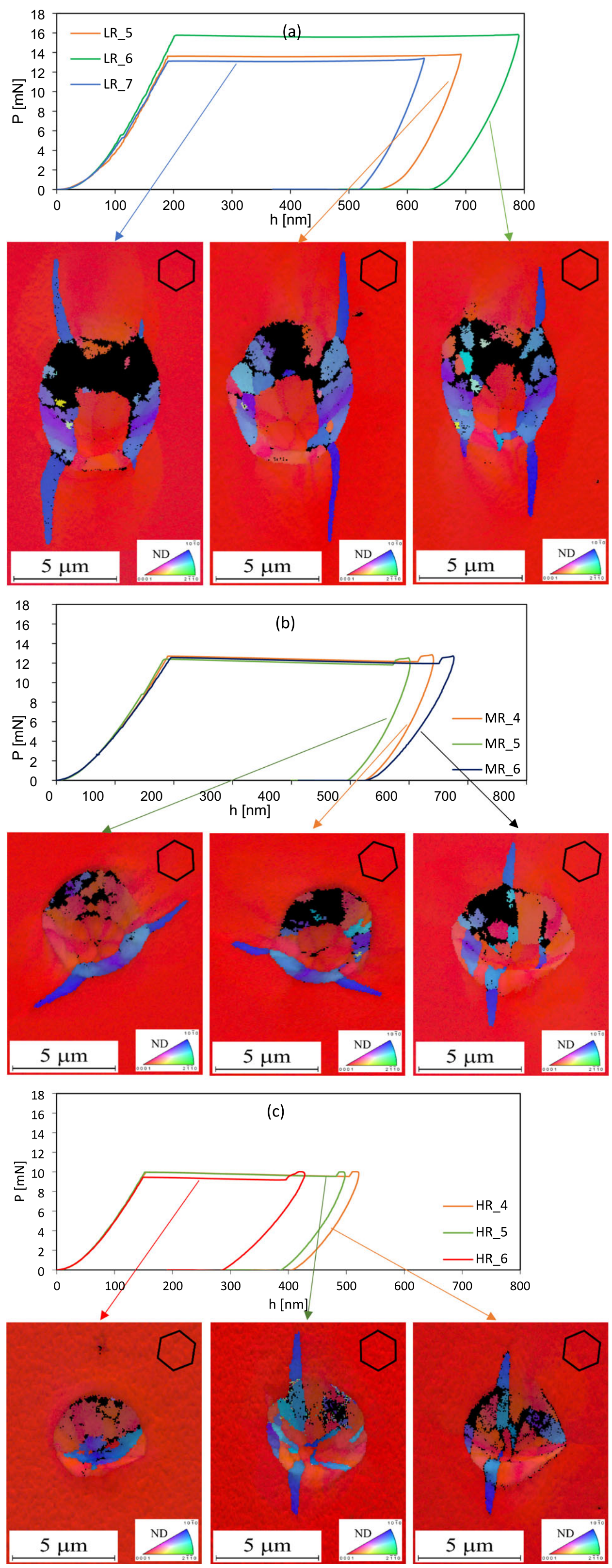

◀Fig. 8—*P-h* curves of exemplary indents with very low load after pop-ins, the IPF maps corresponding to individual imprint were assigned by arrow lines of similar colours. (*a*) 0.5 mN/min, (*b*) 5 mN/min, and (*c*) 80 mN/min. The basal plane crystal structure is included in the EBSD maps similarly to Figure 7. Sink-in (and subsequently twin structure) also was created along the $[\bar{1}2\bar{1}0]$ direction.

words, twinning is one of the deformation mechanisms of pop-in events that is always present in our experiments.

As described in the previous section, we recorded a negative correlation between loading rate and pop-in load. This behaviour stands in contrast to the opposite tendency, which is more often reported, where the pop-in load increases with an increment in the loading rate. This difference may stem from the source of the displacement bursts: the majority of the first occurrences of pop-in are associated with nucleation of dislocation loops, whereas in our experiments, pop-in events were formed from a combination of two mechanisms, twinning and dislocation slip. In particular, twinning is a mechanism that is well known in the literature to be rate-sensitive.[50] Deformation by twinning has also been found to be more active at higher loading or strain rates in compression[51] and tension[52] tests, resulting in an increasing volume fraction of twinning. In experiments at lower rates, dislocation slip has been shown to be the dominant or sole mechanism.[52] In Reference 53, Cao *et al.* performed dynamic compression tests of CoCrFeNi high-entropy alloys, together with further analysis using a series of molecular dynamics simulations. The authors presented evidence that twinning deformation can occur earlier (or at lower strain) in tests at higher strain rates than at low strain rates. The negative SRS (drop of hardness with increasing loading rate) in nanoindentation experiments with HCP material was also observed by Yu *et al.*[15] It is possible to reason that the rate-sensitivity characteristic of twin deformation plays a role in the pop-in behaviour; in other words, the twin system is activated at a lower penetration depth for high loading rate indents, leading to an early displacement burst.

The occurrence of twin deformation early can be due to the short time for material to deform, such that a drastic and large deformation mechanism such as compression twin was needed to accommodate the change in the applied displacement. Whereas for lower loading rates, the crystal structure would have more time to orient itself, or dislocation slip is adequate for plastic deformation.

It worth nothing that the twin structure presented in the previous chapter, more particularly in section C, developed to such a scale during pop-in event, within a very small window of time, almost instantaneously. In other words, in our experiment, one effect of different loading rates on twin deformation is the delay of twin nucleation, rather than the rate at which twin propagates. For the lowest loading rate indentation, the EBSD measurements displayed qualitatively similar twin structure as manifestation of pop-in events at

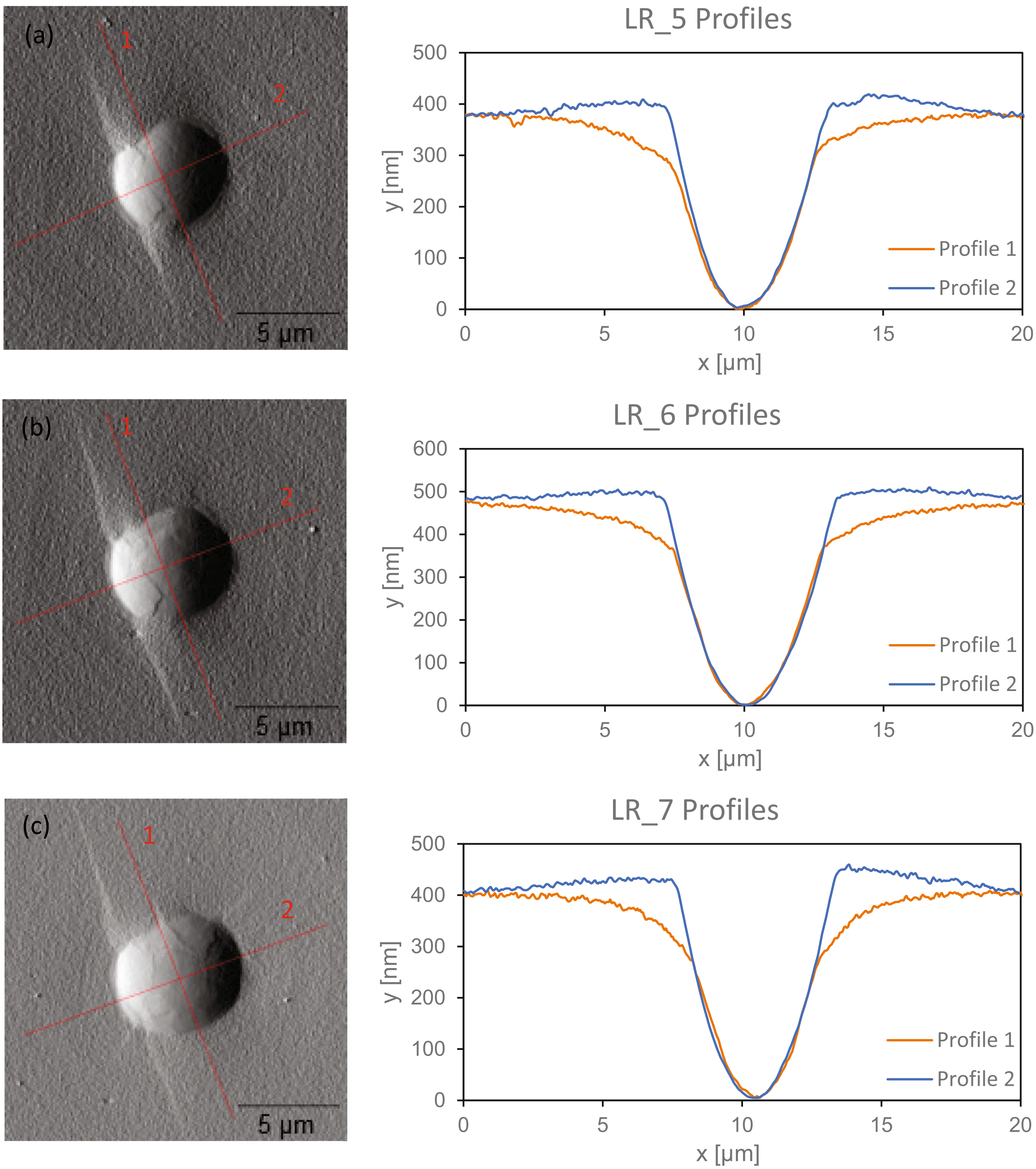

Fig. 9—AFM gradient maps of 0.5 mN/min loading rate imprint shown in Figure 8(a): (*a*) LR_5, (*b*) LR_6 and (*c*) LR_7.

different load and displacement. The medium loading rate indents share some similar features to each other to a lesser extent such as twin structure found in the sink-in direction, while the highest loading rate indents show a more random, less concentrated twin structure. This suggests that the twin deformation is more orderly when the loading rate decreases (at the low loading rate). Furthermore, the pop-in event occurred at the latest in the lowest loading rate experiments, yet the twin structure on the surface was developed the most in these experiments compared to those of other loading rates. The difference in the amount of twin is not as evident between 5 and 80 mN/min loading rates indents.

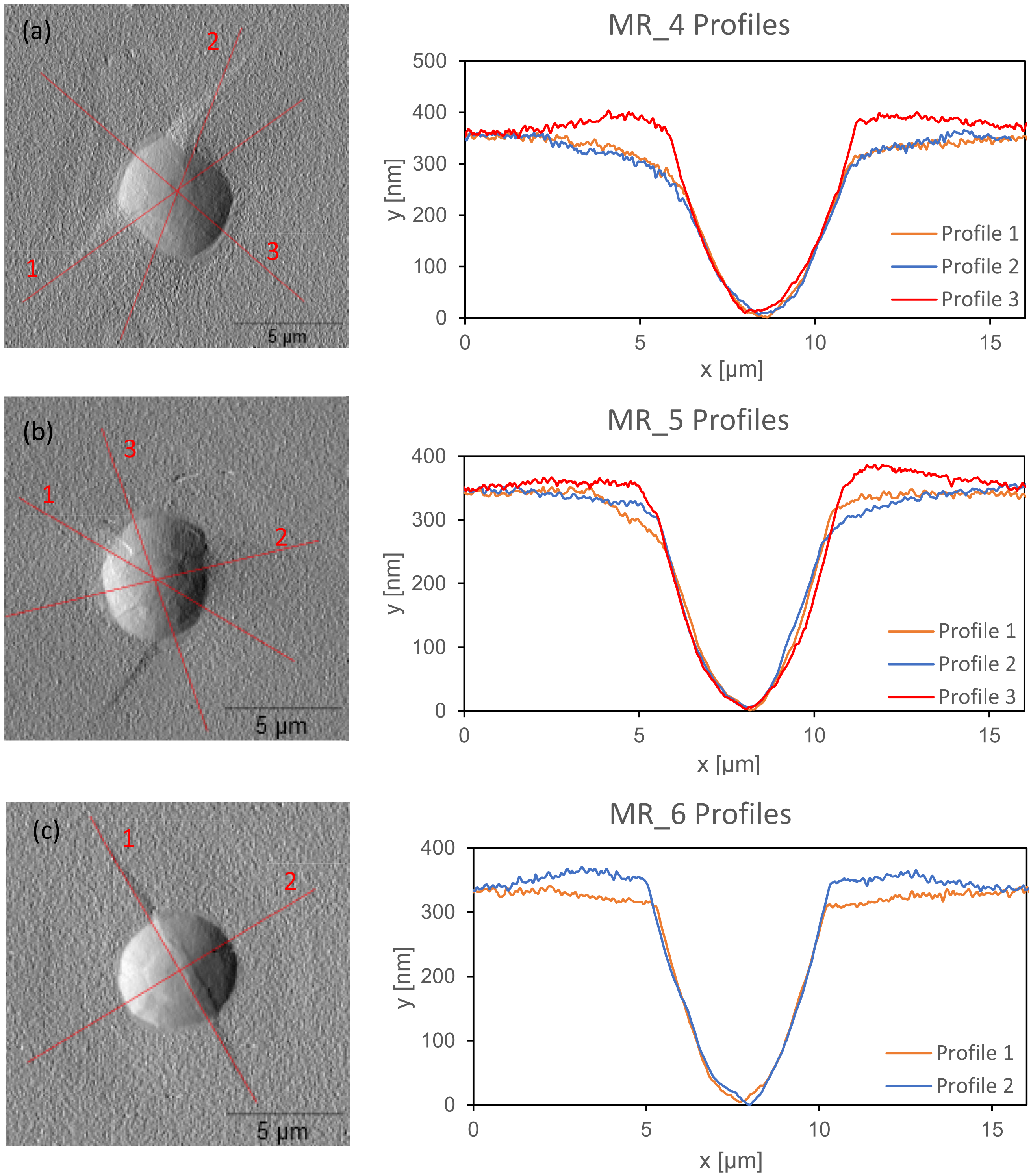

Fig. 10—AFM gradient maps of 5 mN/min loading rate imprint shown in Figure 8(b): (*a*) MR_4, (*b*) MR_5 and (*c*) MR_6.

A conclusion can be reached that at pop-in events, twinning is more active as loading rate increases, yet the twin formation is more limited.

B. *Deformation After Pop-ins*

Imprint HR_1 (Figure 1) is an example of imprint with extensive load after pop-in. In this stage, the material is in fully plastic regime and *P*-*h* curve is composed of at least two different segments with dissimilar slopes. Accordingly to the solution presented in References 54, 55, for spherical indentation, the slope of *P*-*h* curve in fully plastic mode can be correlated with effective plastic hardening of the indented material. In References 54, 55, it was shown that for rigid-plastic, isotropic material whose uniaxial, true stress–strain

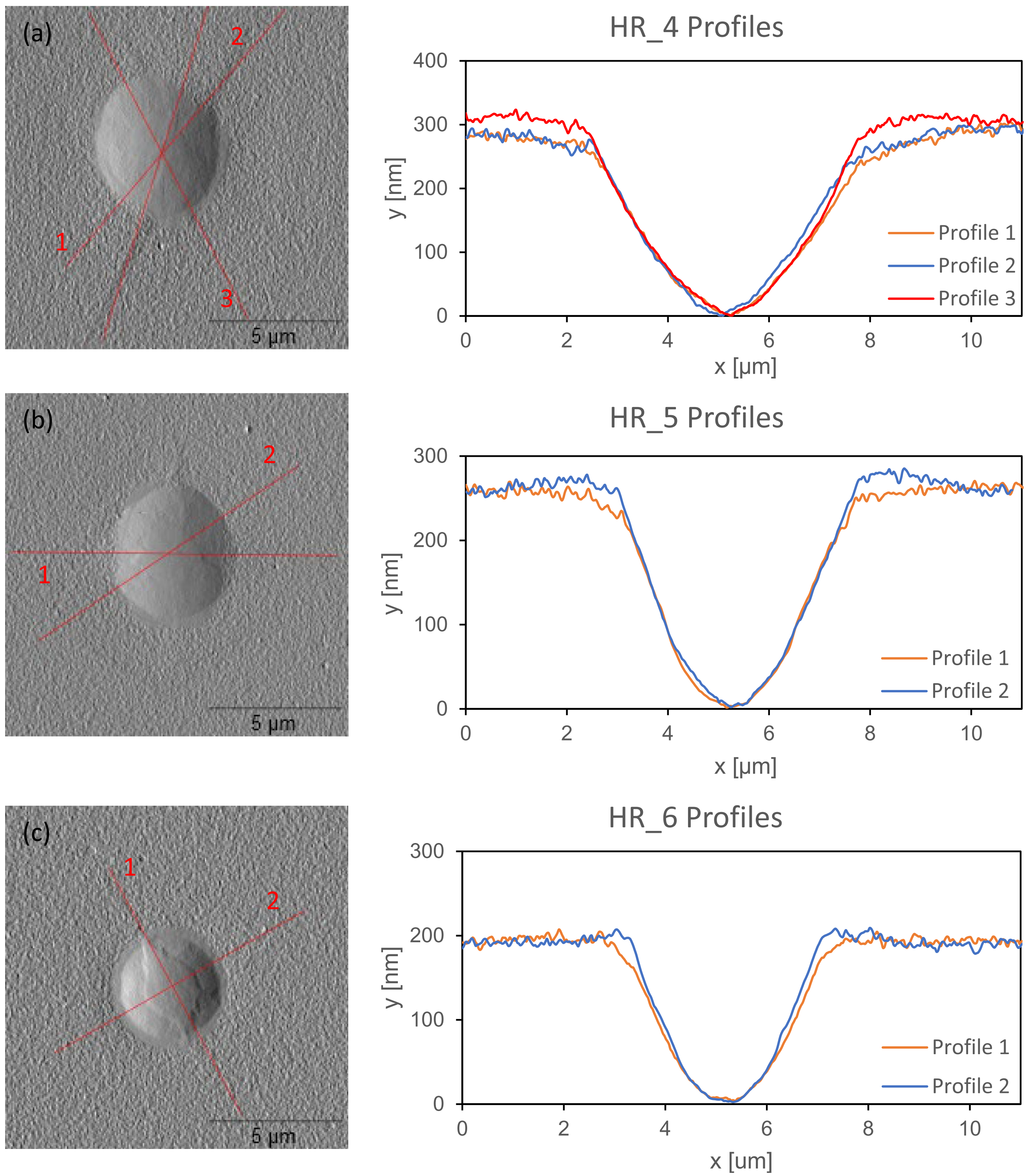

Fig. 11—AFM gradient maps of 80 mN/min loading rate imprint shown in Figure 8(c): (*a*) HR_4, (*b*) HR_5 and (*c*) HR_6.

curve has the form $\sigma \sim k\varepsilon^m$, the indentation *P*-*h* curve has a form $P \sim kh^{m/2+1}$ (*m* is hardening exponent). On the basis of this solution, it can be seen that, when the material exhibits strain hardening ($m > 0$), the *P*-*h* curve is concave and a change in strain hardening is associated with a change in the inclination and curvature of the *P*-*h* curve. When the material exhibits strain hardening or is perfectly plastic ($m \geq 0$), the *P*-*h* curve has no inflection points; so the derivative of the *P*-*h* curve is either constant or increases continuously with an increase in *P*. The inflection points observed after pop-in in our results should be correlated with a drop of hardening parameter *m* or the coefficient *k* at a certain stage of deformation. The key assumption here is that the

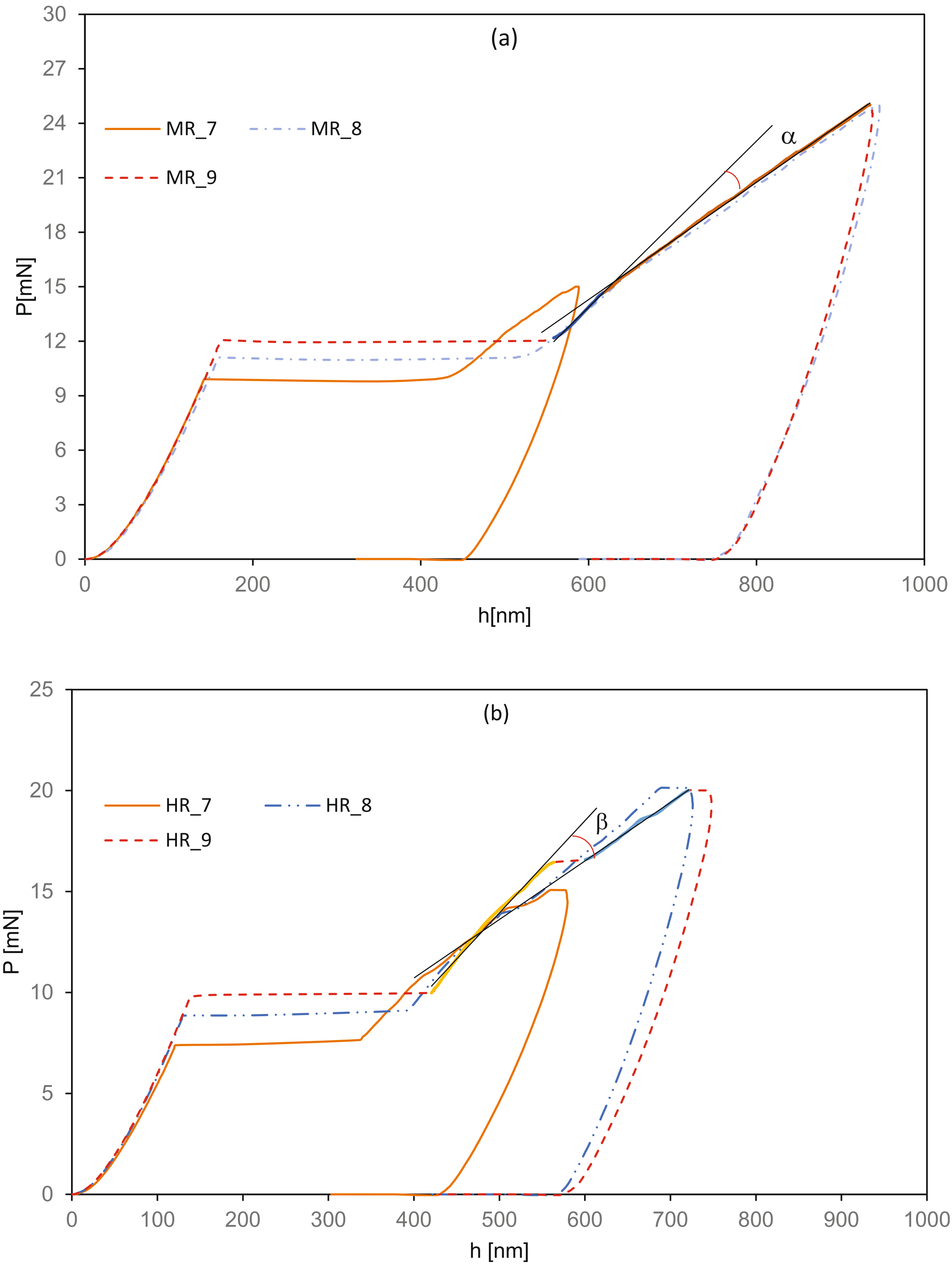

Fig. 12—Indentation curves for loading rates: (*a*) 5 and (*b*) 80 mN/min with high maximum load after pop-in event. For each group, one indent was chosen to illustrate the portion of the *P*-*h* curve after pop-in to have segments of different slopes. α and β are angles between different slopes for lower and higher loading rate indents, respectively, to further highlight the difference between segments.

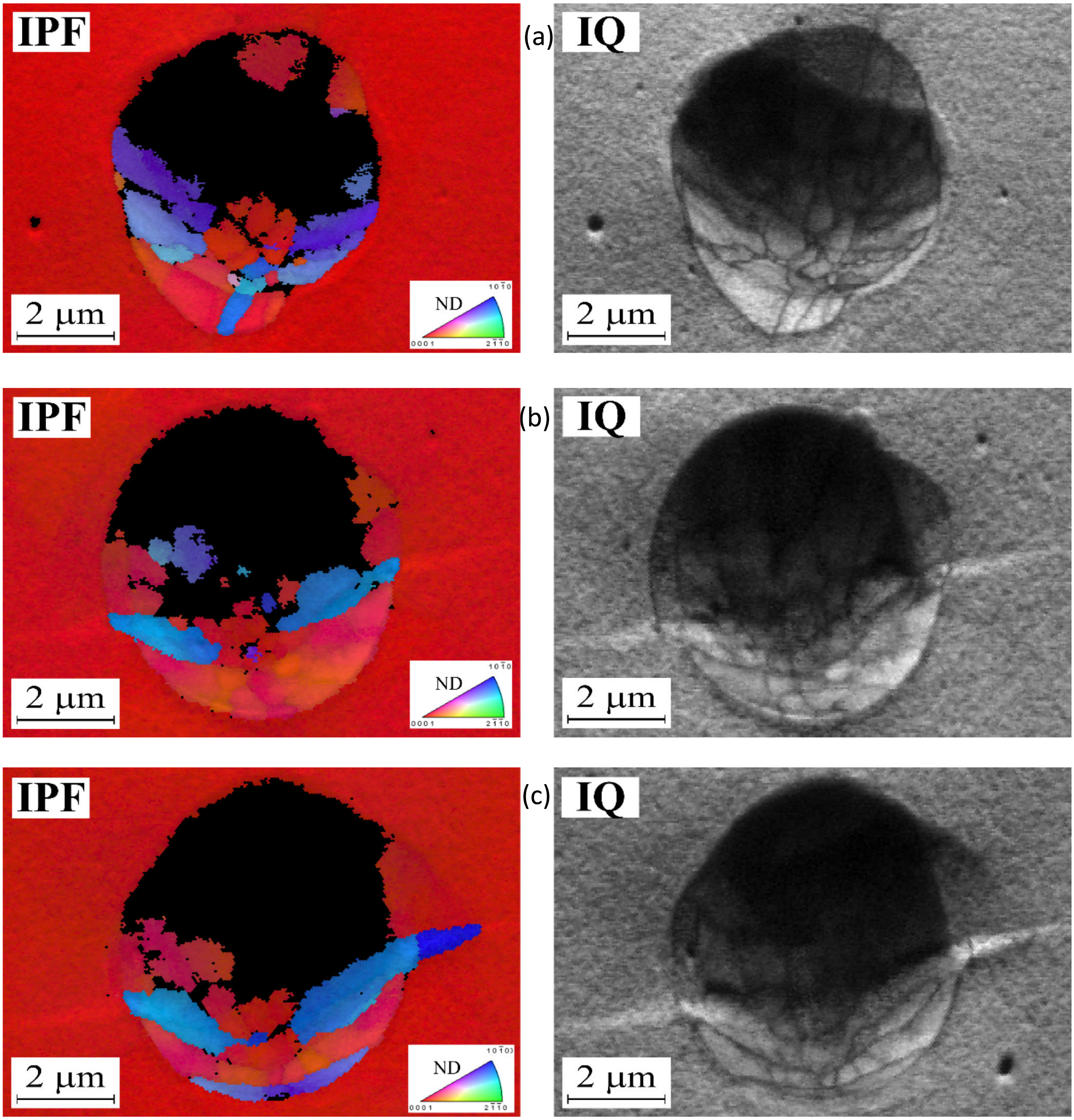

Fig. 13—Maps for the residual impressions obtained from EBSD measurements: misorientation map and image quality map, (*a*) MR_9, (*b*) HR_8 and (*c*) HR_9.

solution is valid for relatively low penetration depths ($a/R < 0.2$), where a and R are the radius of contact and the tip radius, respectively. This assumption is met in our tests. Therefore, when the load increases after pop-in, the loading curves in Fig. 12 change from a higher strain hardening stage to lower strain hardening stage. It is worth noting that this corresponds to an effective hardening, which is the result of a combination of twinning and/or slip activity on different slip systems beneath the indenter.

The transition in work hardening tendency may or may not correspond to a minor pop-in. In the case where a displacement burst takes place, the induced displacement should be smaller than 15 nm; unfortunately, this was not captured due the low acquisition rate set in some of our tests. This change in strain hardening is not seen in most of the examples in Figure 1, as the majority of the indents shown here have the set maximum load that is close to their respective pop-ins, such that the loading curves do not enter the next stage where the material is softer.

Some similarities to this deformation behaviour can be found in the data reported by Sarker and Chen in Reference 56 from compression tests of an extruded Mg–Al–Mn (AM 30) alloy, as well as Salem *et al*.[57,58] for Ti samples. Although the experimental results collected by these authors involved a polycrystalline sample, in our case after the first major pop-ins, as demonstrated above, the contact areas were fragmented into cells or subgrains at the micro or sub-micro scale rather than retaining the single-crystal structure. Hence, it is reasonable that our results can be interpreted similarly.

In References 56 through 58, strain hardening was categorised into three separate stages. The first stage (A) involved a decrease in strain hardening rate, which was attributed to twin nucleation and the subsequent increase in twin volume fraction in the material. In our nanoindentation tests, this stage was not observed, and no direct correlation could be made. Although twins could be detected after pop-in events, this phenomenon occurred in a much shorter time and was almost instantaneous. In contrast, the experiments of Sarker and Chen were done at a rather slow rate of $1.25 \times 10^{-4}\ s^{-1}$; meanwhile, the loading rate in References 57, 58 was $0.01\ s^{-1}$, suggesting that the twins were dynamically developed over a greater span of time. In the subsequent stage (B), there was an increase in strain hardening rate. This trend was explained in terms of the formation of the twin structure at the prior stage impeding the movement of dislocations, due to the discontinuity of slip systems, which could lead to a potential dislocation pile-up at the twin boundary.[50,59] This stage was followed by a decrease in strain hardening rate or a softer behaviour in stage C. The change from a stiffer to a softer behaviour (which is illustrated with trend lines of different slopes corresponding to each section for one indent per figure) is illustrated in Figures 12(a) and (b) for medium and high loading rate indents, respectively.

The authors in References 56, 57, 58 provided different mechanisms for this phenomenon. In Reference 56, the author proposed that a continuous decrease in the twin volume or twin boundary density due to detwinning leads to a reduction in overall resistance to the dislocation movements of twin cells. In References 57, 58, the transition to softer behaviour upon increased load or strain is attributed to the saturation of twin deformation in hcp materials, such as titanium. It could be gathered from these studies that for materials that plastically deform by twinning, the change to a softer behaviour is correlated to a change in twinning behaviour as further load is applied.

We can find an indirect confirmation of these observations in our tests. EBSD measurements were taken for imprints with a high increase in load after pop-in during medium and high loading rate tests (Figure 13). A comparison of these imprints with those corresponding to immediate unloading after the initial pop-in, Figures 8(b), (c), shows that the contact boundary continues to expand, while the length and width of the sink-in created outside the contact boundary during the initial pop-in remain almost constant. Therefore, when the load exceeds the pop-in load, it appears that the external twin (the bird's wing) does not increase in size. Instead, it is gradually 'engulfed' by the expanding contact area and appears inside the contact boundary in the final configuration.

For the medium loading rate, Figure 13(a), twin structure does not alter greatly in the direction of the bird wing. However, the other twin cell on the opposite side in the residual impression appears to be larger than those in Figure 8(b) for imprints of low increase of load after pop-ins. Similar twin cells were found in the MR_2 imprint (low increase in load after pop-in) [Figure 7(d)], although more regions deformed by slip were observed for this imprint. The current evidence suggests there is an increase in twin fraction as the indent is loaded further from the pop-in event for medium loading rate.

For high loading rate, Figure 13(b), (c), the main twin cells observed inside the contact area are longitudinal in shape, running in the direction of the bird's wings. They were therefore most likely generated during the pop-in process and were not increased by subsequent loading remaining quite similar to the cells in indent HR_4 and HR_5 [Figure 8(c), the comparison was made between these imprints due to their similar pop-in loads]. Outside of the direction of the sink-in, there are a few smaller in size cells scattered on the surface. At this stage, the area fraction of twin cells appears to be smaller than immediately after pop-in. The reduction in twin fraction may cause a decrease in hardening after pop-in, as observed in the P-h curves in Figure 12(b). This would be consistent with the explanation presented in Reference 56, cited above.

V. CONCLUSION

The effect of loading rate on pop-in events in nanoindentation experiments on single-crystal zinc has been systematically investigated by using three different loading rates. The following conclusions can be drawn from the work done here:

- The complex twin/slip cells structure is generated in single crystal almost instantaneously during pop-in event for all three loading rate experiments.
- The occurrence of pop-in events in nanoindentation experiments on single-crystal zinc is found to be sensitive to the loading rate. There is a negative correlation between the pop-in initiation load and loading rate, i.e. pop-in events are more likely to occur at lower loads for imprints at higher loading rates.
- Twin deformation is found to be one of the mechanisms for pop-in events for all three experiment loading rates.
- The delay in pop-in event can be attributed to the rate sensitivity of twinning to loading rates. In more detail, for higher loading rate indentation, twinning occurs at lower load and the twin area fracture decreases. The lowest loading rate imprints have the largest area of twin on the surface. The twin structure becomes more ordered as the loading rate

decreases. At the lowest loading rate, the twin structure has very similar features, despite the difference in pop-in loads and displacements within the maximum load range of 18mN.

– The *P-h* curves recorded when the load increases after the pop-in event exhibits a discontinuous change in slope, which corresponds to a change in the material's stiffness (usually a decrease). It is hypothesised that this transition to a less stiff stage may be linked to decrease in twin area fraction for high loading rate; however, this hypothesis requires additional testing and will be a focus of future work.

DATA AVAILABILITY

Data will be made available on request.

CONFLICT OF INTEREST

On behalf of all authors, the corresponding author states that there is no conflict of interest.

OPEN ACCESS

REFERENCES

1. M. Goken, R. Sakidja, W.D. Nix, and J.H. Perepezko: *Mater. Sci. Eng. A*, 2001, vol. 319–321A, pp. 902–08. https://doi.org/10.1016/S0921-5093(01)01086-3.
2. D.A. Lucca, M.J. Klopfstein, R. Ghisleni, and G. Cantwell: *CIRP Ann.*, 2001, vol. 51(1), pp. 483–86. https://doi.org/10.1016/S0007-8506(07)61566-2.
3. C.A. Schuh and A.C. Lund: *J. Mater. Res.*, 2004, vol. 19(7), pp. 2152–58. https://doi.org/10.1557/JMR.2004.0276.
4. C.A. Schuh, J.K. Mason, and A.C. Lund: *Nat. Mater.*, 2005, vol. 4, pp. 617–21. https://doi.org/10.1038/nmat1429.
5. H. Bei, Y.F. Gao, S. Shim, E.P. George, and G.M. Pharr: *Phys. Rev. B*, 2008, https://doi.org/10.1103/PhysRevB.77.060103.
6. C. Zhu, Z.P. Lu, and T.G. Nieh: *Acta Mater.*, 2013, vol. 61(8), pp. 2993–3001.
7. J.K. Mason, A.C. Lund, and C.A. Schuh: *Phys. Rev. B*, 2006, vol. 73, pp. 0541021-14. https://doi.org/10.1103/PhysRevB.73.054102.
8. W. Wang, C.B. Jiang, and K. Lu: *Acta Mater.*, 2003, vol. 51(20), pp. 6169–80. https://doi.org/10.1016/S1359-6454(03)00436-1.
9. Q. Zhang, J. Qiao, Y. Zhao, J. Jang, and U. Ramamurty: *Acta Mater.*, 2025, vol. 288, pp. 120826-2–12.
10. Z. Li, X. Jin, Q. Zhang, A. Lan, and J. Qiao: *Mater. Sci. Eng. A*, 2025, vol. 948A, p. 149268.
11. X.K. Zhang, J.C. Huang, P.H. Lin, W.S. Chuang, T.Y. Liu, Y.C. Wu, Y.C. Liao, S. Jason, and C. Jang: *Mater. Sci. Eng. A*, 2020, vol. 775A, p. 138969. https://doi.org/10.1016/j.msea.2020.138969.
12. H. Somekawa and C.A. Schuh: *Acta Mater.*, 2011, vol. 59(20), pp. 7554–63. https://doi.org/10.1016/j.actamat.2011.08.047.
13. I.-C. Choi, Y.-J. Kim, Y. Morris Wang, U. Ramamurty, and J. Jang: *Acta Mater.*, 2013, vol. 61, pp. 7313–23. https://doi.org/10.1016/j.actamat.2013.08.037.
14. D. Chrobak, K.-H. Kim, K.J. Kurzydłowski, and R. Nowak: *Appl. Phys. Lett.*, 2013, vol. 103, pp. 0721011-4. https://doi.org/10.1063/1.4818260.
15. S. Yu, Y. Wan, C. Liu, Z. Chen, and X. Zhou: *Materials*, 2021, vol. 14, pp. 71041-16. https://doi.org/10.3390/ma14227104.
16. L. Wang, H. Bei, T.L. Li, Y.F. Gao, E.P. Gao, E.P. George, and T.G. Nieh: *Scr. Mater.*, 2011, vol. 65(3), pp. 179–82. https://doi.org/10.1016/j.scriptamat.2011.03.036.
17. K.V. Rajulapati, M.M. Biener, J. Biener, and A.M. Hodge: *Philos. Mag. Lett.*, 2010, vol. 90, pp. 35–42. https://doi.org/10.1080/09500830903356893.
18. M.M. Biener, J. Biener, A.M. Hodge, and A.V. Hamza: *Phys. Rev. B*, 2007, vol. 76B, pp. 1654221-6. https://doi.org/10.1103/PhysRevB.76.165422.
19. D. Catoor, Y.F. Gao, J. Geng, M.J.N.V. Prasad, E.G. Herbert, K.S. Kumar, G.M. Pharr, and E.P. George: *Acta Mater.*, 2013, vol. 61, pp. 2953–65. https://doi.org/10.1016/j.actamat.2013.01.055.
20. J. Cheng, T. Guo, and M.R. Barnett: *J. Magnes. Alloys*, 2022, vol. 10, pp. 169–79. https://doi.org/10.1016/j.jma.2021.06.021.
21. R.H. Wagoner: *Metall. Trans. A*, 1984, vol. 15A, pp. 1265–71.
22. J. Shin and M. Pharr: *Scr. Mater.*, 2025, vol. 259, pp. 1165411-6. https://doi.org/10.1016/j.scriptamat.2025.116541.
23. N. P. T. Nguyen, F. Abbès, B. Abbès, and Y. Li: *Proceedings of the International Conference on Advances in Computational Mechanics 2017*, 1st ed., Springer, Phu Quoc Island, Vietnam, 2017, pp. 157–169.
24. P. T. N Nguyen, F. Abbès, B. Abbès, J.S. Lecomte, and C. Schuman: *IOP Conf. Ser.: Mater. Sci. Eng.*, 2019, vol. 540.
25. R. Sarvesha, A. Gokhale, K. Kumar, N.K. Sharma, J. Jain, and S.S. Singh: *Mater. Sci. Eng. A*, 2020, vol. 776A, pp. 1390641-16. https://doi.org/10.1016/j.msea.2020.139064.
26. A.R. Gokhale, R. Sarvesha, R. Prasad, S.S. Singh, and J. Jain: *J. Eng. Mater. Technol.*, 2019, vol. 141(4), pp. 151–54. https://doi.org/10.1016/j.matlet.2019.03.120.
27. R.R. Tohid and S.J. Bull: *Int. J. Mater. Res.*, 2007, vol. 98(5), pp. 353–59.
28. J.J. Vlassak and W.D. Nix: *J. Mech. Phys. Solids*, 1994, vol. 42(8), pp. 1223–45. https://doi.org/10.1016/0022-5096(94)90033-7.
29. S. Kucharski, V.N. Doan, and M. Maj: *Metall. Mater. Trans. A*, 2025, vol. 56A, pp. 2905–32. https://doi.org/10.1007/s11661-025-07820-6.
30. D.C. Miller, M.J. Talmage, and K. Gall: *J. Mater.*, 2006, vol. 21(10), pp. 2480–92. https://doi.org/10.1557/jmr.2006.0303.
31. T.L. Li, Y.F. Gao, H. Bei, and E.P. George: *J. Mech. Phys. Solids*, 2011, vol. 59(6), pp. 1147–62. https://doi.org/10.1016/j.jmps.2011.04.003.
32. H. Bei, E.P. George, J.L. Hay, and G.M. Pharr: *Phys. Rev. letter.*, 2005, vol. 95, pp. 0455011-4. https://doi.org/10.1103/PhysRevLett.95.045501.
33. L. Zhang and T. Ohmura: *Phys. Rev. Lett.*, 2014, vol. 112, pp. 1455041-5. https://doi.org/10.1103/PhysRevLett.112.145504.
34. W.W. Gerberich, S.K. Venkataraman, H. Huang, S.E. Harvey, and D.L. Kohlstedt: *Acta Metal.*, 1995, vol. 43(4), pp. 1569–76. https://doi.org/10.1016/0956-7151(94)00351-H.
35. C. Shin and S. Shim: *J. Mater. Res.*, 2012, vol. 27, pp. 2161–66.
36. J.R. Morris, H. Bei, G.M. Pharr, and E.P. George: *Phys. Rev. Lett.*, 2011, vol. 106, pp. 1655021-4. https://doi.org/10.1103/PhysRevLett.106.165502.
37. W.C. Oliver and G.M. Pharr: *J. Mater. Res.*, 1992, vol. 7, pp. 1564–83.

38. K. Miyahara, S. Matsuoka, and N. Nagashima: *JSME Int. J. Ser. A*, 1998, vol. 41A(4), pp. 562–68. https://doi.org/10.1299/jsmea.41.562.
39. A. Gouldstone, H.J. Koh, K.Y. Zeng, A.E. Giannakopoulos, and S. Suresh: *Acta Mater.*, 2000, vol. 48(9), pp. 2277–95. https://doi.org/10.1016/S1359-6454(00)00009-4.
40. S. Pathak, J.L. Riesterer, S.R. Kalidindi, and J. Michler: *Appl. Phys. Lett.*, 2014, vol. 105, 161913.
41. S. Pathak, D. Stojakovic, R. Doherty, and S.R. Kalidindi: *J. Mater. Res.*, 2009, vol. 24, pp. 1142–55.
42. S. Pathak, J. Shaffer, and S.R. Kalidindi: *Scr. Mater.*, 2009, vol. 60(6), pp. 1142–55. https://doi.org/10.1016/j.scriptamat.2008.11.028.
43. S. Kucharski and S. Woźniacka: *Metall. Mater. Trans. A*, 2019, vol. 50A, pp. 2139–54. https://doi.org/10.1007/s11661-019-05160-w.
44. Z. Ma, S. Long, Y. Pan, and Y. Zhou: *J. Mater. Sci.*, 2008, vol. 43, pp. 5952–55. https://doi.org/10.1007/s10853-008-2838-0.
45. Y.L. Chiu and A.H.W. Ngan: *Acta Mater.*, 2002, vol. 50, pp. 1599–1611. https://doi.org/10.1016/S1359-6454(02)00025-3.
46. D.F. Bahr, D.E. Kramer, and W.W. Gerberich: *Acta Mater.*, 1998, vol. 46, pp. 3605–17. https://doi.org/10.1016/S1359-6454(98)00024-X.
47. N.I. Tymiak, D.E. Kramer, D.F. Bahr, J.T. Wyrobek, and W.W. Gerberich: *Acta Mater.*, 2001, vol. 49, pp. 1021–34. https://doi.org/10.1016/S1359-6454(00)00378-5.
48. G. Nayyeri, W.J. Poole, C.W. Sinclair, S. Zaefferer, P.J. Konijnenberg, and C. Zambaldi: *Mater. Sci. Eng. A*, 2016, vol. 670A, pp. 132–45. https://doi.org/10.1016/j.msea.2016.05.112.
49. M.H. Yoo: *Metall. Trans. A*, 1981, vol. 12A, pp. 409–18.
50. J.W. Christian and S. Mahajan: *Prog. Mater. Sci.*, 1995, vol. 39, pp. 1–157. https://doi.org/10.1016/0079-6425(94)00007-7.
51. T. Wang, B. Li, M. Li, Y. Li, Z. Wang, and Z. Nie: *Mater Charact*, 2015, vol. 106, pp. 218–25. https://doi.org/10.1016/j.matchar.2015.05.016.
52. Y. Tanaka, M. Kondo, N. Miyayaki, and R. Ueji: *J. Phys.: Conf. Ser.*, 2009, vol. 240.
53. T. Cao, Z. Qian, L. Wang, L. Wang, Y. Xiao, Y. Jiahao, H. Liu, Y. Ren, J. Liang, Y.F. Xua, and X. Li: *Acta Mater.*, 2023, vol. 260, 119343https://doi.org/10.1016/j.actamat.2023.119343.
54. S. Biwa and B. Storakers: *J. Mech. Phys. Solids*, 1995, vol. 43(8), pp. 1303–33.
55. R. Hill, B. Storakers, and A.B. Zdunek: *Proc. R. Soc. Lond.*, 1989, vol. 423, pp. 301–30.
56. D. Sarker and D.L. Chen: *Scr. Mater.*, 2012, vol. 67(2), pp. 165–68. https://doi.org/10.1016/j.scriptamat.2012.04.007.
57. A.A. Salem, S.R. Kalidindi, R.D. Doherty, and S.L. Semiatin: *Metall. Mater. Trans. A*, 2006, vol. 37A, pp. 259–68. https://doi.org/10.1007/s11661-006-0171-2.
58. A.A. Salem, S.R. Kalidindi, and R.D. Doherty: *Acta Mater.*, 2003, vol. 51, pp. 4225–37. https://doi.org/10.1016/S1359-6454(03)00239-8.
59. C. Tromas, S. Parent, W. Sylvain, L. Thilly, G. Renou, C. Zehnder, S. Schröders, S. Korte-Kerzel, and A. Joulain: *Acta Mater.*, 2022, vol. 227, 117665https://doi.org/10.1016/j.actamat.2022.117665.